Antimicrobial mitochondrial reactive oxygen species induction by lung epithelial metabolic reprogramming

Authors: Yongxing Wang[1], Vikram V. Kulkarni[1,2], Jezreel Pantaleón García[1], Miguel M. Leiva-Juárez[1], David L. Goldblatt[1], Fahad Gulraiz[1], Jichao Chen[1], Sri Ramya Donepudi[2], Philip L. Lorenzi[2], Hao Wang[3], Lee-Jun Wong[3], Michael J. Tuvim[1], Scott E. Evans[1,2*]

Affiliations:

[1]Department of Pulmonary Medicine, University of Texas MD Anderson Cancer Center, Houston, Texas, USA

[2]University of Texas MD Anderson Cancer Center UTHealth Graduate School of Biomedical Sciences, Houston, Texas, USA

[3]Department of Bioinformatics and Computational Biology, University of Texas MD Anderson Cancer Center, Houston, Texas, USA

[4]Molecular and Human Genetics, Baylor College of Medicine, Houston, Texas, USA

*Corresponding author. Email: seevans@mdanderson.org.

Abstract: Pneumonia is a worldwide threat, making discovery of novel means to combat lower respiratory tract infections an urgent need. We have previously shown that manipulating the lungs' intrinsic host defenses by therapeutic delivery of a unique dyad of pathogen-associated molecular patterns protects mice against pneumonia in a reactive oxygen species (ROS)-dependent manner. Here we show that antimicrobial ROS are induced from lung epithelial cells by interactions of CpG oligodeoxynucleotides (ODNs) with mitochondrial voltage-dependent anion channel 1 (VDAC1) without dependence on Toll-like receptor 9 (TLR9). The ODN-VDAC1 interaction alters cellular ATP/ADP/AMP localization, increases delivery of electrons to the

electron transport chain (ETC), enhances mitochondrial membrane potential ($\Delta\psi_m$), and differentially modulates ETC complex activities. These combined effects promote leak of electrons from ETC complex III, resulting in superoxide formation. The ODN-induced mitochondrial ROS yield protective antibacterial effects. Together, these studies identify a therapeutic metabolic manipulation strategy that has the potential to broadly protect patients against pneumonia during periods of peak vulnerability without reliance on currently available antibiotics.

Author Summary: Pneumonia is a major cause of death worldwide. Increasing antibiotic resistance and expanding immunocompromised populations continue to enhance the clinical urgency to find new strategies to prevent and treat pneumonia. We have identified a novel inhaled therapeutic that stimulates lung epithelial defenses to protect mice against pneumonia in a manner that depends on production of reactive oxygen species (ROS). Here, we report that the induction of protective ROS from lung epithelial mitochondria occurs following the interaction of one component of the treatment, an oligodeoxynucleotide, with the mitochondrial voltage-dependent anion channel 1. This interaction alters energy transfer between the mitochondria and the cytosol, resulting in metabolic reprogramming that drives more electrons into the electron transport chain, then causes electrons to leak from the electron transport chain to form protective ROS. While antioxidant therapies are endorsed in many other disease states, we present here an example of therapeutic induction of ROS that is associated with broad protection against pneumonia without reliance on administration of antibiotics.

INTRODUCTION

Pneumonia has long been recognized as a leading cause of death among healthy and immunosuppressed people worldwide (1-3). Pneumonia management has historically focused on patient-extrinsic factors, such as antibiotic administration (4, 5). To address such challenges as increasing antibiotic resistance and newly emerging infections, our laboratory focuses on manipulating vulnerable patients' intrinsic antimicrobial defenses to broadly protect them against pneumonia. We advance a strategy of activating the lungs' mucosal defenses to induce broad, pathogen-agnostic protection via airway delivery of synthetic Toll-like receptor (TLR) agonists.

Once regarded as simple airflow conduits or inert gas exchange barriers, the airway and alveolar epithelia are critical immune effector cells that supplement the lungs' mucosal immune defenses by undergoing fundamental structural and functional changes upon encountering pathogens (6-8). These cells sense pathogens via pattern recognition receptors (PRRs), modulate lung leukocyte responses through cytokine and chemokine expression, and release microbicidal molecules such as reactive oxygen species (ROS) and antimicrobial polypeptides (AMPs) (9-11). Harnessing this defensive immune function, we developed a protective PRR agonist therapeutic comprised of a synthetic diacylated lipopetide ligand for TLR2/6 (Pam2CSK4, "Pam2") and a class C unmethylated CpG oligodeoxynucleotide ligand for TLR9 (ODN M362, "ODN"). A single inhaled treatment with this non-intuitive dyad of ligands ("Pam2-ODN") for spatially segregated TLRs yields substantial protection against pneumonia (12-16).

We recently reported that Pam2-ODN-induced antimicrobial protection requires therapeutic induction of ROS from both mitochondrial and dual oxidase sources (17, 18), but the molecular mechanisms responsible for inducible antimicrobial ROS generation remained unresolved. Here, we find that ODN induces mitochondrial ROS (mtROS) production via metabolic reprogramming that alters mitochondrial electron transport chain (ETC) activity in a mitochondrial membrane potential ($\Delta\psi_m$)-dependent manner. These findings provide novel

insights into development of metabolic strategies to protect against otherwise lethal pneumonias in vulnerable populations.

RESULTS

Induction of epithelial mtROS by CpG ODN

Having reported that Pam2 and ODN M362 are both required for maximal antimicrobial protection in a manner that depends on inducible ROS production from both mitochondria and dual oxidases, we sought to determine which ligand(s) induce mtROS production. As shown in Figure 1A, ODN M362 alone induced as much mtROS generation as the Pam2-ODN combination from human lung epithelial (HBEC3-KT) cells, revealing ODN M362 as the main driver of this response. This capacity to induce mtROS was not common to all nucleic acid treatments (Figure 1A), but was observed following treatment of HBEC-3KT cells with various types of oligodeoxynucleotides (Figure 1B). Similarly, ODN M362 mtROS in mouse lung epithelial (MLE-15) cells (Figure 1C), as well as primary human and mouse lung epithelial cells (Figure 1D-E), regardless of which mtROS detector was used (Figure S1). Fluorescence microscopy of primary lung epithelial cells from mice expressing redox-sensitive mitochondrial GFP (mt-roGFP) (19, 20) revealed that, at baseline, mitochondria display a predominantly reduced GFP phenotype, whereas treatment with ODN induces a predominantly oxidized mitochondrial phenotype (Figure 1F-G). Under normal conditions, oxidative phosphorylation consumes >95% of cellular oxygen (21), but mtROS formation also requires free oxygen (22). By inhibiting oxidative phosphorylation with oligomycin, we demonstrate increased oxygen consumption by superoxide (O_2-•) production following ODN (Figure 1H). This ODN-induced mtROS production is consistently associated with increased $\Delta\psi_m$, as assessed by different assays (Figure 1I-K).

CpG ODN alters electron transport chain activity and energy production

mtROS production is tightly regulated by electron transport chain (ETC) activity (23). To understand the mechanisms of ODN-induced mtROS production, we analyzed the enzymatic activity of the ETC complexes in HBEC3-KT cells, finding that that ODN treatment induces a 35% increase in complex II activity and an 82% decrease in complex III activity, along with an increase in citrate synthase activity (Figure 2A, Figure S2). We also found modest but statistically significant reductions in complex V activity, suggesting ODN may interfere with mitochondrial energy production (Figure S2). The change in ETC complex activity was not accompanied by changes in mitochondrial protein concentrations (Figure 2B, Figure S3), suggesting that the ODN effect is mediated by manipulating ETC function rather than altering mitochondrial mass.

Since the major energy output of ETC activity is ATP, we investigated the impact of ODN treatment on cellular ATP levels. ODN treatment caused a rapid decline in whole-cell ATP concentrations with a nadir around 30 min that recovered by 90 min (Figure 2C). In contrast, cellular ADP and AMP levels persistently rose following ODN exposure (Figure 2D-E). These effects on ATP, ADP and AMP were ODN dose-dependent (Figure S4). A drop-and-recovery pattern similar to that of ATP was seen in cellular NADH levels after ODN treatment, whereas NADPH levels were largely unaffected by ODN treatment (Figure 2F-G, Figure S4). NAD/NADH are electron receptor and donor that links large molecule catabolism to mitochondrial energy production. The congruent temporal patterns of NADH and ATP support a hypothesis that ODN stimulates catabolic reactions related to mitochondrial energy production. In contrast, NADPH is primarily produced in the anabolic pentose phosphate pathway, which ODN does not appear to perturb. Levels of reduced glutathione persistently declined after ODN treatment (Figure 2H), consistent with the continuing production of ODN-induced ROS.

CpG ODN blocks mitochondrial nucleotide transition

As TLR9 is the established intracellular sensor for CpG ODNs (24), we examined whether TLR9 activation regulates ODN-induced mtROS generation. To our surprise, ODN treatment still fully induced mtROS production in primary mouse lung epithelial cells isolated from *Tlr9* knockout mice or from mice lacking downstream TLR signaling molecules MyD88 or TRAF6 (Figure S5), indicating that ODN-induced mtROS generation does not require TLR9 signaling.

Seeking to identify a TLR9-independent mechanism by which ODN alters mitochondrial energy metabolism, we investigated whether ODNs could directly stimulate mtROS production in isolated mitochondria. Remarkably, we found that direct ODN treatment of mitochondria isolated from HBEC3-KT cells recapitulates the inducible mtROS generation and increased ΔΨm observed in whole cells (Figure 3A-B). Alternately, to examine whether ODN interacts with mitochondria in intact cells, whole cells were treated with fluorescently-labeled ODN, then the mitochondria were isolated and assessed for fluorescence intensity. As in Figure 3C, mitochondria from cells treated with labeled ODN displayed significant fluorescence, supporting a hypothesis that ODN can directly interact with mitochondria to stimulate mtROS production. To identify potential mitochondrial ODN binding partners, HBEC3-KT cells were treated with biotin-labeled ODN, then the streptavidin precipitants from mitochondria lysates were resolved on an SDS PAGE gel. The silver stain in Figure 3D demonstrates bands present only after ODN treatment. The boxed area was excised and liquid chromatography–mass spectrometry proteomic analysis generated a list of candidate targets.

Among the most differentially detected peptides was voltage-dependent anion-sensitive channel 1 (VDAC1), an outer mitochondrial membrane protein component of the VDAC1-ANT1-mCK complex that regulates exchange of ATP and ADP between the mitochondria and cytosol (25, 26). In targeted pulldown studies in mouse and human cells, we confirmed that VDAC1 was

detected in immunoprecipitated samples of biotinylated ODN treated cells (Figure 3E-F, Figure S6). The association of ODN with VDAC1 increased with treatment time. We also detected association of ODN with adenine nucleotide translocator 1 (ANT1), the inner mitochondrial membrane component of the VDAC1-ANT1-mCK complex (Figure 3G, Figure S6). When HBEC3-KT cells were treated with fluorescently labeled ODN then VDAC1 was localized with fluorescently labeled antibody (Figure 3H), 75% of pixels occupied by VDAC1 were also occupied by ODN. The mean Pearson's correlation coefficient between ODN and VDAC1 pixel intensity was 0.84 (Figure S7), indicating a high degree of colocalization in intact cells.

Given the role of the VDAC1-ANT1-mCK complex as an ATP:ADP antiporter, we investigated whether altered ATP/ADP localization might account for the changes in whole-cell energy stores previously observed following ODN treatment (Figure 2C-E). Indeed, we found that ODN treatment causes mitochondrial ATP levels to rapidly increase and cytosolic ATP levels to precipitously decline, with the opposite pattern for ADP and AMP (Figure 3I), consistent with a ODN-induced blockade of ATP:ADP antiporter function. To test whether VDAC1 antagonism can explain the ODN effect on mitochondrial energy metabolism, we investigated the effects of a known VDAC1 inhibitor erastin (27, 28) and an ANT1 inhibitor carboxyatractyloside (CAT) (29, 30). Because VDAC1 is one of the subunits composed of the mitochondrial permeability transition pore (mPTP), we also exposed cells to mPTP inhibitor cyclosporin A (31, 32). As shown in Figure 5J-L, erastin and cyclosporin A caused changes in $\Delta\psi_m$, mtROS production, and oxygen consumption that were comparable to ODN, suggesting that blocking VDAC-mediated mitochondrial nucleotide exerts these effects.

AMPK-directed metabolic reprogram increases electron delivery to complex II

AMP-activated kinase (AMPK) is a cellular energy sensor that is activated when cytosolic AMP levels rise due to ATP consumption (33, 34), in turn activating catabolic pathways to promote

ATP production, including acetyl-CoA carboxylase (ACC) (35, 36). Congurent with the observations that ODN alters cellular ATP/ADP/AMP stores (Figures 2-3), reverse phase protein array analysis of HBEC3-KT cells treated with ODN revealed AMPK and ACC to be among the most activated signaling pathways following ODN exposure (Figure 4A). We confirmed time-dependent ODN-induced phosphorylation of AMPKα1, AMPKα2 and ACC in vitro (Figure 4B, Figure S8). Similarly, AMPKα1 phosphorylation was induced by both erastin and cyclosporin A in vitro (Figure 4C, Figure S8). ODN-induced AMPKα phosphorylation was also demonstrated by immunofluorescence staining in mouse airways (Figure 4D-E). When AMPKα genes were conditionally deleted (Figure S9), ODN-inducible mtROS production was significantly reduced without impacting baseline mtROS production (Figure 4F).

A principle means by which AMPK-ACC pathway activation promotes mitochondrial energy production is through increased carnitine palmitoyltransferase 1 (CPT1)-dependent fatty acid β-oxidation. We found that ODN treatment increases acetyl CoA concentrations and fatty acid β-oxidation (Figure 4G-H). Further, treatment of HBEC3-KT cells with etomoxir, an irreversible inhibitor of CPT1 (37, 38), significantly attenuated ODN-induced mtROS production, oxygen consumption and ETC complex II activity (Figure 4I-K). Knockdown of *CPT1* (Figure S10) also attenuated inducible mtROS production to a similar degree to etomoxir (Figure 4L).

Mitochondrial fatty acid β-oxidation generates NADH and $FADH_2$, which contribute electrons to the ETC via electron shuttle proteins. Specifically, $FADH_2$-carried electrons are transferred to coenzyme Q (CoQ) by electron flavoprotein dehydrogenase (ETFDH) (39), while NADH-carried electrons are transferred to complex II by glycerol-3-phosphate dehydrogenase (GPD2) (40). Knocking down either of these shuttles (Figure S10) attenuated ODN-induced mtROS production (Figure 4M-N). Fatty acid β-oxidation also generates acetyl-CoA which transfers electrons to the ETC via the tricarboxylic acid (TCA) cycle. Treatments with TCA intermediate metabolites oxaloacetate and α-ketoglutarate or the analogue dimethyl malonate

attenuated ODN-induced mtROS production (Figure S11). Dimethyl malonate and oxaloacetate are ETC complex II inhibitors while α-ketoglutarate inhibits glutaminolysis (41-43).

In the ETC, $CoQH_2$ is generated when CoQ accepts electrons from $FADH_2$. The $CoQH_2$:CoQ ratio has been described as an indicator of ETC efficiency, with an increased ratio associated with increased mtROS production (44). As in Figure 4O, ODN treatment caused an increase in $CoQH_2$:CoQ ratio. Although augmented β-oxidation is required for maximal ODN-induced mtROS production, inducible mtROS production can also be partially attenuated by inhibiting glycolysis and/or glutaminolysis (Figure S12). Future work will explore the contributions of these pathways.

Together, these results indicated that ODN-induced and AMPK-regulated metabolic reprogramming enhances electron delivery to ETC, increases complex II activity and eventually drives mtROS induction. These findings were schematically summarized in Figure 4P.

ODN-induced mtROS generation at complex III is ΔΨm-dependent

It is intriguing that ODN simultaneously increases complex II activity and decreases complex III activity. We hypothesized that these changes in ETC complex activity might provide insights into the site(s) of mtROS generation. A series of ETC complex inhibitors were used to determine the roles of ETC complexes in ODN-induced mtROS generation.

mtROS are formed when molecular oxygen interacts with an electron leaked among electron transport chain (23), typically from complex I [flavin (F) site and ubiquinone reduction (Q) site] or complex III (Q_o site) (45). Whereas mtROS formation at complex I following other stimuli can be inhibited by rotenone (Q site) or diphenyleneiodonium (F site) (46, 47), neither agent impeded ODN-induced mtROS (Figure S13). Similarly, while TCA cycle input can support reverse election transport from complex II to complex I in the setting of high $\Delta\psi_m$ (48), we found

that neither succinate nor fumarate influence ODN-induced mtROS formation (Figure S11). These findings, along with the modest ODN impact on complex I activity (Figure 2A, Figure S2), indicated that complex I is not a major site of ODN-induced mtROS production. In contrast, while inhibitors of complex II activity reduced ODN-induced mtROS, inhibitors of complex III enhanced ODN-induced mtROS dramatically (Figure S13). We thus concluded that complex III is the main ODN-induced mtROS generating site following forward electron transfer. Additionally, while complex IV inhibition had no impact on mtROS induction, the complex V inhibitor oligomycin decreased ODN-induced mtROS production. As oligomycin treatment collapses mitochondrial membrane potential $\Delta\psi_m$, this result suggested that ODN-induced $\Delta\psi_m$ increases may be required for mtROS formation.

We compared the impacts of ODN and complex III inhibitor antimycin on complex III activity and mtROS induction. Although treatment with antimycin or ODN resulted in similar inhibition of complex III enzymatic activity and initial mtROS production (Figure 5A-B), the two agents function differently. When stigmatellin and myxothiazol inhibit electron transfer from complex III to complex IV by binding the $CoQH_2$ (ubiquinol) oxidation (Q_o) site, antimycin cannot induce further oxygen consumption for superoxide production while ODN still can (Figure 5C). Antimycin can induce rapid induction of mtROS production in intact epithelial cells and isolated mitochondria, but this effect plateaus by 40 min. Conversely, ODN-induced mtROS continued to increase throughout the period of exposure in intact cells and isolated mitochondria, suggesting different mechanisms of mtROS generation (Figure 5D-E). Central to these differences appeared to be their opposing effects on $\Delta\psi_m$. In both whole cell and isolated mitochondria models, ODN induced increased $\Delta\psi_m$ while antimycin reduced $\Delta\psi_m$ below that observed in sham-treated samples (Figure 5F-G). Disrupting $\Delta\psi_m$ with the uncoupler FCCP (Figure 5H-I) significantly impaired ODN-induced mtROS generation and but had little effect on antimycin-induced mtROS generation (Figure 5J-K). FCCP treatment demonstrated that ODN-induced

oxidation of cytochrome b_H is $\Delta\psi_m$-dependent, whereas FCCP did not alter the oxidation of cytochrome b_H in antimycin-treated mitochondria (Figure 5L). Congruently, in isolated mitochondria, FCCP reversed ODN-impaired complex III electron transfer activity but had no such effect on antimycin treated mitochondria (Figure 5M). The generation of ODN-induced mtROS at complex III is graphically displayed in Figure 5N. Under homeostatic conditions, complex III quickly transfers $CoQH_2$-carried electrons to cytochrome c1, which, in turn, transfers the electrons to complex IV. This process facilitates proton pumping across the inner mitochondrial membrane and establishes normal $\Delta\psi_m$ (49, 50). However, ODN-induced increase in $\Delta\psi_m$ hinders the proton pumping, impeding electron transfer at the Q_o and quinone reduction (Q_i) sites. This $\Delta\psi_m$-dependent retardation of electron transfer in complex III, in coordination with an increased forward electron transfer from complex II, increases the likelihood that highly-reactive electrons will “leak” to interact with free oxygen, resulting in increased formation of mtROS, in the form of superoxide, at complex III (51-53).

Thus, while dissecting the process of ODN-induced antimicrobial mtROS formation, we identified that mtROS induction requires both AMPK-directed metabolic reprograming to augment electron delivery to ETC complex II (Figure 4P) and increased $\Delta\psi_m$ to retard electron transfer at complex III (Figure 5N).

mtROS induction stimulates TLR9-independent antimicrobial effects

To demonstrate the protective effects of antimicrobial mtROS induced by ODN, we have shown that scavenging mtROS by mitoTEMPO or mitoQ (Figure S14) significantly decreases the bacterial killing induced by Pam2-ODN combined treatment in HBEC3-KT cells (18). While pre-treatment with either an ETC complex II inhibitor TTFA or the $\Delta\psi_m$ uncoupler FCCP alone inhibited ODN-induced mtROS to some extent, TTFA-FCCP combination treatment maximally inhibited mtROS production in HBEC3-KT cells (Figure S15) and reversed the mitochondrial

reduced:oxidized ratio of ODN-treated cells (Figure 6A-B). As shown in Figure 6C and Figure S15, the bacterial killing induced by Pam2 and ODN was obviated in HBEC3-KT cells when the cells were pretreated with TTFA-FCCP. Congruently, wild type mice with impaired lung epithelial mtROS generation due to aerosolized TTFA-FCCP pretreatment prior to treatment with Pam2 and ODN were less protected against *P. aeruginosa* pneumonia than were mice who received sham aerosol pretreatment prior to receiving Pam2-ODN (Figure 6D). Notably, both the Pam2-ODN-induced *P. aeruginosa* pneumonia protection and the TTFA-FCCP-induced impairment were observed in *Tlr9* knockout mice (Figure 6E). Consistent with our prior reports (17), airway delivery of TTFA-FCCP had no observed systemic effects on the mice in the absence of infection (Figure 6E). In light of our data supporting VDAC1 blockade as central mediator of protection, we tested whether erastin substituted for ODN could protect against infection. In combination with Pam2, erastin and ODN induced comparable bacterial killing by HEBC3-KT cells (Figure 6F). Strikingly, when delivered by aerosol with Pam2, erastin yielded a similar survival advantage to ODN following *P. aeruginosa* pneumonia challenge in mice (Figure 6G). Even when delivered without Pam2, both ODN and erastin induced significant reductions in the lung bacterial burden (Figure 6H).

In summary, we found that antimicrobial mtROS are generated from lung epithelial cells following ODN treatment. ODN interacts with VDAC1 to alter mitochondrial nucleotide transport, driving AMPK-ACC-CPT1-mediated electron delivery to ETC complex II and increasing $\Delta\psi_m$ to promote superoxide production at complex III.

DISCUSSION

Synthetic CpG ODNs have been explicitly developed as immunomodulators and adjuvants (24, 54, 55). ODN CpG motifs mimic naturally-occurring pathogen-associated molecular patterns recognized by TLR9 that initiate NF-κB-dependent antimicrobial signaling cascades (56-58).

Here, we report previously unknown, TLR9-independent induction of immunometabolic reprogramming by ODN that results in generation of pneumonia-protective mtROS.

ODN-induced mtROS formation is fundamentally a manifestation of altered energy metabolism. ODN interacts with VDAC1 and ANT1 localized in the mitochondrial membranes. The VDAC1-ANT1-mCK complex regulates the exchange of metabolites between the mitochondria and cytosol (25, 26). We show that VDAC1 binding ODN perturbs cellular nucleotide distribution, activating the AMPK-ACC pathway, and promoting fatty acid β-oxidation. Fatty acid β-oxidation augments $FADH_2$-carried electron flux to the ETC by ETFDH, GPD2, and the TCA cycle, all converging on the CoQ pool ($CoQH_2$ and CoQ). Disruption of any of these elements leads to decreases in inducible mtROS generation.

The increased electron delivery as a consequence of AMPK-ACC activation results in increased complex II activity, however, these observations do not resolve why complex III activity are decreased. During normal bifurcated electron transfer in complex III (59, 60), semiquinone (SQ•-) intermediates forming at the Qo or Qi site instantaneously transfer electrons to the low potential heme b (bL) or CoQ, minimizing electron leakage. However, under certain conditions, accumulation of $SQ^{\bullet-}$ increases electron leak (51). In one example, antimycin inhibits CoQ reduction at the Q_i site, leading to electron accumulation on cytochrome b hemes, allowing $SQ^{\bullet-}$ more time to interact with molecular oxygen to form superoxide at the Q_o site (61, 62). Alternatively, high $\Delta\psi_m$ attenuates the proton pump, retarding electron transfer and sustaining cytochrome b hemes in reduced states that cause accumulation of $SQ^{\bullet-}$ at the Q_o and Q_i sites (52, 63). Here, our findings support the latter as the responsible mechanism as uncoupling $\Delta\psi_m$ with FCCP reduces ODN-induced mtROS and reverses ODN-impaired complex III activity. Thus, $\Delta\psi_m$ accentuation by VDAC-perturbed ATP accumulation in mitochondria increases mtROS production and impairs complex III activity.

Although ROS production is often regarded as an untoward cellular event that contributes to degenerative diseases (64, 65), there is robust evidence that controlled mtROS generation contributes to critical signaling events in a wide range of physiologic processes that extend host survival (66-70), including by augmentation of protective antimicrobial responses (71-73). Superoxide formed at the complex III Q_o site may be particularly well suited to function as a cytosolic signaling molecule, as the Q_o site is adjacent to the intermembrane space with about half of its superoxide diffusing to the cytoplasmic side of the inner membrane (74, 75). Here, we demonstrate that complex III-dependent mtROS induction is required for maximally ODN-induced bacterial killing in vitro and in vivo. Although the current work does not explicitly test whether mtROS directly kill pathogens or act as cell signals to initiate antimicrobial responses, both topics are areas of active investigation now.

In summary, we identify metabolic mechanisms underlying the ODN-induced antimicrobial mtROS formation. Under physiologic conditions, mtROS production is exquisitely tightly regulated, but we show here that therapeutic manipulation of mtROS is achievable, protective against otherwise lethal infections, and well tolerated by the host. Indeed, this intervention has also been safely tested in five completed human trials (NCT04313023, NCT04312997, NCT03794557, NCT02566252, NCT02124278) with more in preparation. Because of our interest in pneumonia, all of the current work is performed in lung epithelial cells, but we anticipate similar responses can be detected in other epithelial cells and, likely, other cell types.

METHODS

Primary Cell Cultures and Cell lines

To isolate mouse tracheal epithelial cells (mTECs), mice were anesthetized and tracheas were excised and digested in 1.5 mg/ml Pronase overnight at 4 ºC. mTECs were harvested by centrifugation and then cultured on collagen coated tissue culture plates or transwells in Ham's F12 media supplemented with differentiation growth factors and hormones as previously described (76).

Normal human bronchial epithelial (NHBE) cells were purchased from American Type Culture Collection (ATCC, Manassas, VA) and cultured in airway epithelial cell basal medium supplemented with bronchial epithelial cell growth kit (ATCC, Manassas, VA).

Immortalized Human bronchial epithelial (HBEC3-KT) cells were kindly provided by Dr. John Minna. Murine lung epithelial (MLE-15) cells were kindly provided by Dr. Jeffrey Whitsett. HBEC3-KT and MLE-15 cells were authenticated by the UT MD Anderson Characterized Cell Line Core Facility and IDEXX Bioresearch (Columbia, MO), respectively. HBEC3-KT cells were cultured in keratinocyte serum-free medium supplemented with human epidermal growth factor and bovine pituitary extract (Thermo Fisher Scientific, Grand Island, NY). MLE-15 cells were cultured in DMEM/F2 medium supplemented with 2% of fetal bovine serum and 0.5% of Insulin-Transferrin-Selenium (Thermo Fisher Scientific, Grand Island, NY). Cell cultures were maintained in the presence of 1% of penicillin/streptomycin and glutamine. All cells were cultured at 37 °C with 5% CO_2. All human cell experiments were performed in accordance with Institutional Review Board of The University of Texas MD Anderson Cancer Center (MDACC).

Mice

Wild type C57BL/6J mice were purchased from The Jackson Laboratory (Bar Harbor, ME). *Prkaa1*^{fl} and *Prkaa2*^{fl} mice were purchased from Jackson. *TLR9*$^{-/-}$ mice were provided by Dr. Shizuo Akira (77). *CMV mt-roGFP* mice were generated by Dr. D James Surmeier and kindly

365 provided by Dr. Farhad Danesh (19, 20). *Sftpc-Cre* mice were kindly provided by Dr. Brigid
366 Hogan (78). All mouse experiments were performed in accordance with the MDACC Institutional
367 Animal Care and Use Committee.

368

369 **In Vivo Infection Model**

370 As previously described (8, 18), 10 ml of combined 4 μM Pam2CSK4 and 1 μM ODN M362 in
371 1× phosphate-buffered saline (PBS) was placed in an Aerotech II nebulizer (Biodex, Shirley,
372 NY) and delivered to unrestrained mice in an exposure chamber via an influx polyethylene tube.
373 Nebulization was driven by 10 L/min air supplemented with 5% CO_2. The exposure chamber
374 connects with an identical efflux polyethylene tube with a low resistance microbial filter (BB50T,
375 Pall, East Hills, NY) at its end vented to a biosafety hood.

376 *Pseudomonas aeruginosa* strain PA103 was purchased from ATCC and stored as frozen stock
377 (1×10^8 colony-forming unit CFU/ml) in 20% glycerol in Luria-Bertani (LB) medium. Typically, 1
378 ml of frozen stock was incubated overnight in 100 ml of Tryptic Soy Broth (TSB) at 37°C with
379 5% CO_2, then expanded in 1 liter of fresh LB media at 37°C to OD 600 of 0.52. Bacterial
380 suspensions were centrifuged, washed, re-suspended in 1× PBS, and aerosolized using the
381 same nebulization system for Pam2-ODN treatment. For all bacterial challenges, a nebulized
382 inoculum of 10 ml of ~2×10^{10} CFU/ml were delivered. If not specified, 6 to 8 weeks old single
383 sex mice were used for in vivo infection conducted in a BSL2 biohazard lab. Immediately
384 following bacterial challenge, some mice were anesthetized and mouse lungs were harvested
385 and homogenized using a Mini-Beadbeater-1 (Biospec, Bartlesville, OK). The lung
386 homogenates were used to count lung colony-forming units (CFUs). The remaining mice were
387 closely monitored for 12 days. The relevant euthanasia-triggering criteria consist of any
388 evidence of distressed behaviors including hypothermia, impaired mobility, respiratory distress,
389 and inability to access food or water. When mice were identified to meet the criteria, they were

subjected to euthanasia immediately. At least 8-10 mice per condition were evaluated for survival analysis, 4 mice per condition were sacrificed for pathogen burden assessment. Challenges were performed a minimum of 3 times.

In Vitro Pathogen Killing Assay

HBEC3-KT cells or MLE-15 cells were cultured on 6-well plates in complete media until cell growth reached ~80% confluence. Cells were replaced with fresh, antibiotic-free media containing PBS, Pam2, ODN or Pam2-ODN. The final concentrations of Pam2 or ODN in media were 2.4 µM or 0.6 µM, respectively. 4 h after the treatment, 20 µl of *P. aeruginosa* PA103 (1×10^5 CFUs/ml) were added to each culture well. 4 h after bacteria inoculation, 20 µl of supernatant from each well was aspirated, serially diluted, plated on a TSB agar plate and incubated for 16 h at 37 °C. Bacterial CFUs were counted after the incubation (18). Studies were performed a minimum of 3 times with 4 biological replicates per condition.

Mitochondrial ROS Detection, Scavenging and Inhibition

To detect mtROS generation, cells were incubated with 5 µM of each indicated detector, MitoSOX red, ROSstar 550, MitoTracker Red CMXRos or tetramethylrhodamine (TMRM) in a black-walled, clear bottomed 96-well plate for 1/2 h before ODN or PBS treatment (17). After fluorescent mtROS detectors were washed off, fluorescence was continuously measured on a BioTek Synergy2 plate reader for 3 h immediately after ODN or PBS addition. Excitation/emission wavelengths for mtROS-detecting agents are 510 nm/580 nm. Studies were performed a minimum of 3 times with 8 biological replicates per condition.

To scavenge mtROS, HBEC3-KT cells were exposed to 100 nM MitoTEMPO or 10 µM MitoQ for 1 h prior to fluorescent mtROS detector incubation and ODN or PBS treatment.

To disrupt mtROS production, HBEC3-KT cells were exposed to compounds that inhibit mitochondria electron transport chain activity. These include rotenone (10 μM), TTFA (200 μM), atpenin (10 nM), antimycin (100 nM & 5 μM), sodium azide (1 μM), oligomycin (2 μM) and FCCP (400 nM) etc., for 1 h prior to fluorescent mtROS detector incubation and ODN or PBS treatment. Inhibition of ODN-induced mtROS generation in vitro was achieved by concurrent application of TTFA (200 μM) and FCCP (200 nM).

To inhibit mtROS generation in vivo, mice were exposed to TTFA (200 mM) and FCCP (800 μM) in 10 ml of 50% DMSO solution in 1× PBS by nebulization. The 50% DMSO solution was nebulized as vehicle control. Mice received TTFA-FCCP or vehicle control were treated with either Pam2-ODN or PBS and then subjected to *P. aeruginosa* PA103 challenge.

JC-1 Assay

To monitor changes in mitochondria membrane potential ($\Delta\psi_m$) upon ODN treatment, HBEC3-KT cells were incubated with 2 μM of JC-1 fluorescence dye for 30 min. After the JC-1 dye was washed off, fluorescence was continuously measured with ODN or PBS treatment using a BioTek Synergy2 plate reader at wavelengths of 510nm/580nm for J-aggregates and 490nm/525nm for J-monomers. A higher ratio of J-aggregates to J-monomers indicates a higher $\Delta\psi_M$. To inhibit mitochondrial membrane polarization, TTFA (200 μM) and FCCP (200 nM) were concurrently applied for 1 h before JC-1 incubation and ODN or PBS treatment. Studies were performed a minimum of 3 times with 8 biological replicates per condition.

Indirect Immunofluorescence Assay and Co-localization Image Analysis

PBS or ODN-treated HBEC3-KT cells or MLE-15 cells growing on a chambered coverglass or frozen lung sections from PBS or ODN-treated mice were fixed with 2% paraformaldehyde,

permeabilized with 0.1% Triton X-100, and blocked with 2% goat serum in 1× PBS. Cells or lung sections were incubated with primary antibodies against Phospho-AMPKα-1,2 or VDAC1 at a dilution of 1:200 for 1 h, then with AlexaFluor secondary antibodies (Life Technologies, Carlsbad, CA) at a dilution of 1:500 for half an hour, and counterstained with 4′,6-diamidino-2-phenylindole (DAPI) for 15 minutes. Cells were visualized using a DeltaVision deconvolution fluorescence microscope (GE Life Sciences). Fluorescence intensity of microscope images was quantified using ImageJ.

Pixel intensity data of VDAC1 and ODN-FITC in the fluorescence images were imported into MATLAB and all analysis was performed using default settings. Confidence intervals were set at the 95% confidence limit. Pixel intensity values for VDAC1 and ODN-FITC were compared directly on a scatterplot. Six independent analyses were performed. A simple linear regression model using the least squares standard approach was fit to the data. Pearson's correlation coefficients were calculated to determine whether VDAC1 pixel intensity tended to accumulate with ODN-FITC pixel intensity.

Live Cell Fluorescence Imaging

Fluorescent measurement of intracellular mtROS generation was carried out on live and metabolically active mTECs generated from *CMV mt-roGFP* mice. Cells growing on collagen coated chambered coverglass were mounted onto microscopic chamber at 37 °C in air with 5% CO_2, treated with ODN or PBS and washed with 1× live cell imaging buffer (Life Technologies). CellMask DeepRed was added to stain the cell membrane. Images were obtained using a DeltaVision deconvolution fluorescence microscope (GE Life Sciences) at excitation wavelengths of 405nm and 488nm at 100 minutes post ODN treatment. Fluorescence intensity of microscope images was quantified using ImageJ software.

462

463 **Measurement of Oxygen Consumption Rate**

464 Oxygen consumption rate (OCR) was measured using a Seahorse XFe96 extracellular flux
465 analyzer (Agilent, Santa Clara, CA). HBEC3-KT cells (1.5×10^4 per well) were seeded into a
466 XFe96 microplate and grew overnight in complete media. 1 h before the assay, the media was
467 changed to Seahorse XF assay media (Agilent) and incubated in a non-CO_2 incubator at 37 °C.
468 The microplate was loaded onto the analyzer and basal respiration in these cells were recorded
469 by real-time measurement of OCR. Then 25 µl of PBS, ODN and/or mitochondria inhibitors
470 prepared in the assay medium were sequentially injected into each culture well (in 150 µl of
471 assay media) via drug delivery ports. The final working concentrations of these testing regents
472 in culture wells are ODN 1.2 µM, oligomycin 10 nM, and antimycin 1 µM. After injection of each
473 regent, OCR was again measured. At the end of the assay, the number of viable cells was
474 determined using trypan blue. OCR measurements were normalized to final cell numbers. OCR
475 is expressed in pmole min^{-1}. Studies were performed a minimum of 3 times with 12 biological
476 replicates per condition.

477

478 **Western Blotting and Immunoprecipitation**

479 HBEC3-KT cells or MLE-15 cells were suspended in NP-40 lysis buffer containing Halt protease
480 and phosphatase inhibitor cocktail (Millipore), disrupted by sonication, and extracted at 4°C for
481 30 min. The protein concentration of the lysate was determined using bicinchoninic acid (BCA)
482 protein assay (Pierce). 50 µg protein in 1× Laemmli buffer was separated by SDS-PAGE and
483 then transferred onto polyvinylidene difluoride (PVDF) membranes (Millipore). The PVDF
484 membranes were blotted with primary antibodies, detected by secondary antibodies with
485 conjugated horseradish peroxidase, and developed using a Pico-sensitive chemiluminescence

kit (Pierce). All membranes were stripped and re-blotted for β-actin or GAPDH as loading control.

Whole cell or mitochondria lysates were prepared with biotinylated ODN-treated HBEC3-KT cells or MLE-15 cells. To precipitate proteins Bound by biotinylated ODN in vivo, streptavidin beads (Pierce) were incubated with whole cell or mitochondria lysates containing 300 µg protein overnight at 4° C under constant gentle rotating. After incubation, streptavidin beads were centrifuged, washed with 1× PBS containing 0.05% Tween-20, resuspended in 50 µl of 2× SDS loading buffer, and boiled for 10 minutes. Elutes from the streptavidin beads were loaded onto SDS PAGE gel (Bio-Rad) and immunoblotted with VDAC1 or ANT1 antibody.

Lentiviral shRNA Knockdown

GIPZ *E. coli* clones containing human *CPT1A*, *GPD2* and *ETFDH* lentiviral shRNA vectors were purchased from GE Dharmarcon (Lafayette, CO). The lentiviral shRNA vectors were purified using a QIAGEN plasmid kit. Lentiviruses bearing human *CPT1A*, *GPD2* or *ETFDH* shRNA were produced by co-transfection of the lentiviral shRNA vectors and lentiviral packaging vectors in 293T cells. The shRNA lentiviruses were collected and added into HBEC3-KT cell culture. Lentivirus-infected HBEC3-KT cells were selected by cell sorting based on GFP expression 3 days after infection. Efficiency of the shRNA knockdown was determined by immunoblot using anti-human *CPT1A*, *GPD2* or *ETFDH* antibodies.

Adenoviral Cre Knockout

Adenovirus containing Cre recombinase or control empty vectors were purchased from Viral Vector Core at the University of Iowa. As previously described (79), adenoviral infections were carried out in mTECs derived from *Prkaa1*$^{fl/fl}$;*Prkaa2*$^{fl/fl}$ mice.

Mitochondria Isolation

Mitochondria were isolated from either excised mouse lungs or harvested HBEC3-KT or MLE-15 cells. As previously described (80), a Polytron homogenizer (Pro Scientific, Oxford, CT) was used to dissociate tissues and cells. Mitochondria were separated from cytosol via serial centrifugation at 4 °C. The concentration of the isolated mitochondria was normalized in between PBS or ODN treatment groups using BCA protein assay (Pierce). The isolated mitochondria were maintained in mitochondrial isolation buffer on ice for further analysis.

Biochemical Analysis of Mitochondrial Complex Activity

As previously described (81), spectrophotometric analysis of the respiratory chain complexes was performed on HBEC3-KT cells collected at the indicated time points after ODN treatment. The electron transport chain enzymes were assayed at 30° C using a temperature-controlled spectrophotometer (Ultraspec 6300 pro, Biochrom Ltd., Cambridge, England). The activities of complex I (NADH:ferricyanide reductase), complex II (succinate dehydrogenase), rotenone sensitive complex I+III (NADH:cytochrome c reductase), complex II + III (succinate:cytochrome c reductase) and complex IV (cytochrome c oxidase) were measured using appropriate electron acceptors/donors (82, 83). The increase or decrease in absorbance of cytochrome c at 550 nm was measured for complex I + III, II + III, or complex IV. The activity of NADH:ferricyanide reductase was measured by oxidation of NADH at 340 nm. For succinate dehydrogenase, the reduction of 2,6-dichloroindophenol (DCIP) was measured at 600 nm. For citrate synthase, the reduction of dithionitrobenzoic acid (DTNB) was measured at 412 nm. Enzyme activities are expressed in nmol/min/mg protein. Complex III activity was measured using a Mitochondrial

Complex III activity assay kit (BioVision). Complex V activity was measured using a Quantichrom ATPase assay kit (Bioassay Systems).

Luminescence Glo Assay

HBEC3-KT cells (1×10^4 per well) were plated in an opaque-walled 96-well plate and grown overnight. Cells were treated with 0.6 µM ODN and collected at various time points after treatment. Cells were lysed on the plate and incubated with luminescence glo regents per the luminescence glo assay kit's instructions (Promega). Luminescence was recorded using a BioTek Synergy2 plate reader.

Fatty Acid Oxidation Assay

A non-radioactive fatty acid oxidation (FAO) assay kit (Biomedical Research Service, State University of New York at Buffalo) was used to measure FAO activity in ODN-treated HBEC3-KT cells. Cells were lysed and incubated with substrate octanoyl-CoA and then FAO assay solution in a 96-well plate, following the manufacturer's instruction. Oxidation of the octanoyl-CoA by the cell lysate generates NADH, which is coupled to the reduction of the tetrazolium salt INT to formazan in the FAO assay solution. The absorbance of the newly formed formazan (at 490 nm) is proportional to FAO activity.

Coenzyme Q_{10} Measurement by Triple Quadruple LC-MS

Levels of ubiquinone (CoQ_{10}) and ubiquinol (reduced form) in PBS or ODN treated HBEC3-KT cells were measured using an Agilent 6460 triple quadruple mass spectrometer coupled with an Agilent 1290 series HPLC system. PBS or ODN treated cells were quickly washed with ice-cold

PBS and then liquid nitrogen was poured onto cells to rapidly quench metabolic and chemical reactions. To extract ubiquinone and ubiquinol, 100 µl of 100% isopropanol were added and mixed with the cells. Coenzyme Q_9 was added as an internal standard. The cell extracts were vortexed, centrifuged at 17,000 g for 5 minutes at 4 °C, and supernatants were transferred to clean auto sampler vials for direct injection. The mobile phase is methanol containing 5 mM ammonium formate. Ubiquinone, ubiquinol and CoQ_9 were separated on a Kinetex® 2.6 µm C18 100 Å, 100 x 4.6 mm column. The flow rate was 700 µL/min at 37 °C. The mass spectrometer was operated in the MRM positive ion electrospray mode with the following transitions: Ubiquinone/oxidized, m/z 880.7→197.1; Uniquinol/reduced, m/z 882.7→197.1; CoQ_9 (IS), m/z 795.6 →197.1. Raw files were imported and analyzed using Agilent Mass Hunter Workstation software-Quantitative Analysis.

Cytochrome b_H Measurement

The method of cytochrome b_H measurement was adapted from that described by Quinlan et al. (61). Isolated mitochondria (1 mg/ml) were resuspended at 37 °C in buffer containing 120 mM KCl, 5 mM HEPES, 1 mM EGTA (pH 7.2 at 20 °C), and 0.3% (w/v) bovine serum albumin. Absorbance change in Cytochrome b_H was measured after ODN or antimycin A addition using a NanoDrop One UV-Vis spectrophotometer (ThermoFisher Scientific). The Cytochrome b_H signal was recorded by spectrum scanning at the wavelength pair 566–575 nm at 37 °C with stirring and normalized based on the assumption that reductions of b_H are 0% with no added substrate and 100% with saturating substrates plus 2 µM DTT. In parallel with cytochrome b_H measurement, mtROS generation was detected in isolated mitochondria (0.5 mg/ml) treated by ODN or antimycin A using mitoSOX red as above described. To determine the effect of the mitochondria membrane potential on Cytochrome b_H redox state and mtROS generation in

isolated mitochondria, $b_H^{\%red}$ and mtROS were analyzed after addition of 500 nM FCCP in the assay buffer along with ODN or antimycin A treatment.

Proteomics Analysis

The biotinylated ODN-bound proteins were precipitated with streptavidin beads from mitochondria lysates and resolved by PAGE (Bio-rad). The PAGE gels were stained using a silver staining kit (Pierce). Silver-stained gel pieces were excised, washed, destained and digested in-gel with 200 ng modified trypsin (sequencing grade, Promega) and Rapigest (TM, Waters Corp.) for 18 h at 37° C. In-solution samples were precipitated with 5:1 v/v of cold acetone at -20° C for 18 h, then centrifuged and the acetone was removed prior to treatment with Rapigest (100 °C for 10 min), followed by addition of trypsin. The resulting peptides were extracted and analyzed by high-sensitivity LC-MS/MS on an Orbitrap Fusion mass spectrometer (Thermo Scientific, Waltham MA). Proteins were identified by database searching of the fragment spectra against the SwissProt (EBI) protein database using Mascot (v 2.6, Matrix Science, London, UK) and Proteome Discoverer (v 2.2, Thermo Scientific). Typical search settings were: mass tolerances, 10 ppm precursor, 0.8d fragments; variable modifications, methionine sulfoxide, pyro-glutamate formation; enzyme, trypsin, up to 2 missed cleavages. Peptides were subject to 1% FDR using reverse-database searching.

RPPA Analysis

The reverse phase protein array (RPPA) analyses were performed to examine 161 protein targets in PBS or ODN treated HBEC3-KT cells. Cell lysates were serially diluted in 5 two-fold dilutions with RPPA lysis buffer. An Aushon Biosystems 2470 arrayer (Burlington, MA) was used to print lysates on nitrocellulose-coated FAST slides (Schleicher & Schuell BioScience)

and make protein arrays. The array slides were probed with primary antibodies followed by detection with appropriate biotinylated secondary antibodies. The signal was amplified using the Vectastain ABC Elite kit (Vector Laboratories) and visualized by DAB colorimetric reaction. The slides were scanned, analyzed, and quantified using Microvigene software (VigeneTech Inc., Carlisle, MA) to generate spot signal intensities, which were processed by the R package SuperCurve (version 1.01). A fitted “supercurve” was plotted with the signal intensities on the Y-axis and the relative log2 concentration of each protein on the X-axis using the non-parametric, monotone increasing B-spline model (84). Protein concentrations were derived from the supercurve for each lysate by curve-fitting and normalized by median polish (85). Differential protein expression analysis was performed using R with LIMMA package and adjusted for multiple-testing using the Benjamini-Hoechberg method to reduce the false discovery rate.

Quantification and Statistical Analysis

Statistical analyses were performed using SigmaPlot 14.0 (Systat Software, San Jose, CA) and GraphPad Prism 8 (GraphPad Software, San Diego, CA). One-way ANOVA was used to compare the means of multiple treatment conditions or multiple time points. The Holm-Sidak method was used, unless normality testing failed, in which case Kruskall-Wallis method was used. Means of two groups were compared using two-way Student’s t-test. Survival comparisons were performed using logrank testing by the Mantel-Cox approach.

Extended Data and Supplementary Information

Tables S1 to S2

Fig. S1 to S15

References

1. Mizgerd JP. Lung infection--a public health priority. PLoS Med. 2006;3(2):e76.

2. File TM. Community-acquired pneumonia. Lancet. 2003;362(9400):1991-2001.

3. DALYs GBD, Collaborators H. Global, regional, and national disability-adjusted life-years (DALYs) for 333 diseases and injuries and healthy life expectancy (HALE) for 195 countries and territories, 1990-2016: a systematic analysis for the Global Burden of Disease Study 2016. Lancet. 2017;390(10100):1260-344.

4. Bjerre LM, Verheij TJ, Kochen MM. Antibiotics for community acquired pneumonia in adult outpatients. Cochrane Database Syst Rev. 2009(4):CD002109.

5. Niederman MS, Mandell LA, Anzueto A, Bass JB, Broughton WA, Campbell GD, et al. Guidelines for the management of adults with community-acquired pneumonia. Diagnosis, assessment of severity, antimicrobial therapy, and prevention. Am J Respir Crit Care Med. 2001;163(7):1730-54.

6. Leiva-Juarez MM, Kolls JK, Evans SE. Lung epithelial cells: therapeutically inducible effectors of antimicrobial defense. Mucosal Immunol. 2018;11(1):21-34.

7. Evans SE, Xu Y, Tuvim MJ, Dickey BF. Inducible innate resistance of lung epithelium to infection. Annu Rev Physiol. 2010;72:413-35.

8. Cleaver JO, You D, Michaud DR, Pruneda FA, Juarez MM, Zhang J, et al. Lung epithelial cells are essential effectors of inducible resistance to pneumonia. Mucosal Immunol. 2014;7(1):78-88.

9. Bals R, Hiemstra PS. Innate immunity in the lung: how epithelial cells fight against respiratory pathogens. Eur Respir J. 2004;23(2):327-33.

10. Bartlett JA, Fischer AJ, McCray PBJ. Innate immune functions of the airway epithelium. Contrib Microbiol. 2008;15:147-63.

11. Johnston SL, Goldblatt DL, Evans SE, Tuvim MJ, Dickey BF. Airway Epithelial Innate Immunity. Front Physiol. 2021;12:749077.

12. Clement CG, Evans SE, Evans CM, Hawke D, Kobayashi R, Reynolds PR, et al. Stimulation of lung innate immunity protects against lethal pneumococcal pneumonia in mice. Am J Respir Crit Care Med. 2008;177(12):1322-30.

13. Evans SE, Scott BL, Clement CG, Larson DT, Kontoyiannis D, Lewis RE, et al. Stimulated innate resistance of lung epithelium protects mice broadly against bacteria and fungi. Am J Respir Cell Mol Biol. 2010;42(1):40-50.

14. Tuvim MJ, Gilbert BE, Dickey BF, Evans SE. Synergistic TLR2/6 and TLR9 activation protects mice against lethal influenza pneumonia. PLoS One. 2012;7(1):e30596.

15. Duggan JM, You D, Cleaver JO, Larson DT, Garza RJ, Guzman Pruneda FA, et al. Synergistic interactions of TLR2/6 and TLR9 induce a high level of resistance to lung infection in mice. J Immunol. 2011;186(10):5916-26.

16. Evans SE, Tseng CK, Scott BL, Hook AM, Dickey BF. Inducible Epithelial Resistance against Coronavirus Pneumonia in Mice. Am J Respir Cell Mol Biol. 2020;63(4):540-1.

17. Kirkpatrick CT, Wang Y, Leiva Juarez MM, Shivshankar P, Pantaleon Garcia J, Plumer AK, et al. Inducible Lung Epithelial Resistance Requires Multisource Reactive Oxygen Species Generation To Protect against Viral Infections. mBio. 2018;9(3).

18. Ware HH, Kulkarni VV, Wang Y, Pantaleon Garcia J, Leiva Juarez M, Kirkpatrick CT, et al. Inducible lung epithelial resistance requires multisource reactive oxygen species generation to protect against bacterial infections. PLoS One. 2019;14(2):e0208216.

19. Galvan DL, Badal SS, Long J, Chang BH, Schumacker PT, Overbeek PA, et al. Real-time in vivo mitochondrial redox assessment confirms enhanced mitochondrial reactive oxygen species in diabetic nephropathy. Kidney Int. 2017;92(5):1282-7.

20. Guzman JN, Sanchez-Padilla J, Wokosin D, Kondapalli J, Ilijic E, Schumacker PT, et al. Oxidant stress evoked by pacemaking in dopaminergic neurons is attenuated by DJ-1. Nature. 2010;468(7324):696-700.

679 21. Wilson DF, Harrison DK, Vinogradov SA. Oxygen, pH, and mitochondrial oxidative
680 phosphorylation. J Appl Physiol (1985). 2012;113(12):1838-45.
681 22. Zhao RZ, Jiang S, Zhang L, Yu ZB. Mitochondrial electron transport chain, ROS
682 generation and uncoupling (Review). Int J Mol Med. 2019;44(1):3-15.
683 23. Murphy MP. How mitochondria produce reactive oxygen species. Biochem J.
684 2009;417(1):1-13.
685 24. Krieg AM. CpG motifs in bacterial DNA and their immune effects. Annu Rev Immunol.
686 2002;20:709-60.
687 25. Camara AKS, Zhou Y, Wen PC, Tajkhorshid E, Kwok WM. Mitochondrial VDAC1: A Key
688 Gatekeeper as Potential Therapeutic Target. Front Physiol. 2017;8:460.
689 26. Vyssokikh MY, Brdiczka D. The function of complexes between the outer mitochondrial
690 membrane pore (VDAC) and the adenine nucleotide translocase in regulation of energy
691 metabolism and apoptosis. Acta Biochim Pol. 2003;50(2):389-404.
692 27. DeHart DN, Fang D, Heslop K, Li L, Lemasters JJ, Maldonado EN. Opening of voltage
693 dependent anion channels promotes reactive oxygen species generation, mitochondrial
694 dysfunction and cell death in cancer cells. Biochem Pharmacol. 2018;148:155-62.
695 28. Huo H, Zhou Z, Qin J, Liu W, Wang B, Gu Y. Erastin Disrupts Mitochondrial Permeability
696 Transition Pore (mPTP) and Induces Apoptotic Death of Colorectal Cancer Cells. PLoS One.
697 2016;11(5):e0154605.
698 29. Cadenas S, Buckingham JA, St-Pierre J, Dickinson K, Jones RB, Brand MD. AMP
699 decreases the efficiency of skeletal-muscle mitochondria. Biochem J. 2000;351 Pt 2:307-11.
700 30. Haworth RA, Hunter DR. Control of the mitochondrial permeability transition pore by
701 high-affinity ADP binding at the ADP/ATP translocase in permeabilized mitochondria. J
702 Bioenerg Biomembr. 2000;32(1):91-6.

703 31. Karch J, Bround MJ, Khalil H, Sargent MA, Latchman N, Terada N, et al. Inhibition of
704 mitochondrial permeability transition by deletion of the ANT family and CypD. Sci Adv.
705 2019;5(8):eaaw4597.
706 32. Lemasters JJ. Evolution of Voltage-Dependent Anion Channel Function: From Molecular
707 Sieve to Governator to Actuator of Ferroptosis. Front Oncol. 2017;7:303.
708 33. Carling D, Mayer FV, Sanders MJ, Gamblin SJ. AMP-activated protein kinase: nature's
709 energy sensor. Nat Chem Biol. 2011;7(8):512-8.
710 34. Hardie DG. AMP-activated/SNF1 protein kinases: conserved guardians of cellular
711 energy. Nat Rev Mol Cell Biol. 2007;8(10):774-85.
712 35. Marcinko K, Steinberg GR. The role of AMPK in controlling metabolism and
713 mitochondrial biogenesis during exercise. Exp Physiol. 2014;99(12):1581-5.
714 36. Steinberg GR. Role of the AMP-activated protein kinase in regulating fatty acid
715 metabolism during exercise. Appl Physiol Nutr Metab. 2009;34(3):315-22.
716 37. Schlaepfer IR, Joshi M. CPT1A-mediated Fat Oxidation, Mechanisms, and Therapeutic
717 Potential. Endocrinology. 2020;161(2).
718 38. Thupari JN, Pinn ML, Kuhajda FP. Fatty acid synthase inhibition in human breast cancer
719 cells leads to malonyl-CoA-induced inhibition of fatty acid oxidation and cytotoxicity. Biochem
720 Biophys Res Commun. 2001;285(2):217-23.
721 39. Wang Y, Palmfeldt J, Gregersen N, Makhov AM, Conway JF, Wang M, et al.
722 Mitochondrial fatty acid oxidation and the electron transport chain comprise a multifunctional
723 mitochondrial protein complex. J Biol Chem. 2019;294(33):12380-91.
724 40. Chowdhury SK, Gemin A, Singh G. High activity of mitochondrial glycerophosphate
725 dehydrogenase and glycerophosphate-dependent ROS production in prostate cancer cell lines.
726 Biochem Biophys Res Commun. 2005;333(4):1139-45.

727 41. Fendt SM, Bell EL, Keibler MA, Olenchock BA, Mayers JR, Wasylenko TM, et al.
728 Reductive glutamine metabolism is a function of the alpha-ketoglutarate to citrate ratio in cells.
729 Nat Commun. 2013;4:2236.
730 42. Huang LS, Shen JT, Wang AC, Berry EA. Crystallographic studies of the binding of
731 ligands to the dicarboxylate site of Complex II, and the identity of the ligand in the
732 "oxaloacetate-inhibited" state. Biochim Biophys Acta. 2006;1757(9-10):1073-83.
733 43. Kolaj-Robin O, O'Kane SR, Nitschke W, Leger C, Baymann F, Soulimane T. Biochemical
734 and biophysical characterization of succinate: quinone reductase from Thermus thermophilus.
735 Biochim Biophys Acta. 2011;1807(1):68-79.
736 44. Guaras A, Perales-Clemente E, Calvo E, Acin-Perez R, Loureiro-Lopez M, Pujol C, et al.
737 The CoQH2/CoQ Ratio Serves as a Sensor of Respiratory Chain Efficiency. Cell Rep.
738 2016;15(1):197-209.
739 45. Brand MD. The sites and topology of mitochondrial superoxide production. Exp Gerontol.
740 2010;45(7-8):466-72.
741 46. Koopman WJ, Nijtmans LG, Dieteren CE, Roestenberg P, Valsecchi F, Smeitink JA, et
742 al. Mammalian mitochondrial complex I: biogenesis, regulation, and reactive oxygen species
743 generation. Antioxid Redox Signal. 2010;12(12):1431-70.
744 47. Li Y, Trush MA. Diphenyleneiodonium, an NAD(P)H oxidase inhibitor, also potently
745 inhibits mitochondrial reactive oxygen species production. Biochem Biophys Res Commun.
746 1998;253(2):295-9.
747 48. Lambert AJ, Brand MD. Inhibitors of the quinone-binding site allow rapid superoxide
748 production from mitochondrial NADH:ubiquinone oxidoreductase (complex I). J Biol Chem.
749 2004;279(38):39414-20.
750 49. Crofts AR, Hong S, Ugulava N, Barquera B, Gennis R, Guergova-Kuras M, et al.
751 Pathways for proton release during ubihydroquinone oxidation by the bc(1) complex. Proc Natl
752 Acad Sci U S A. 1999;96(18):10021-6.

753 50. Trumpower BL. The protonmotive Q cycle. Energy transduction by coupling of proton
754 translocation to electron transfer by the cytochrome bc1 complex. J Biol Chem.
755 1990;265(20):11409-12.
756 51. Lanciano P, Khalfaoui-Hassani B, Selamoglu N, Ghelli A, Rugolo M, Daldal F. Molecular
757 mechanisms of superoxide production by complex III: a bacterial versus human mitochondrial
758 comparative case study. Biochim Biophys Acta. 2013;1827(11-12):1332-9.
759 52. Lee I, Bender E, Arnold S, Kadenbach B. New control of mitochondrial membrane
760 potential and ROS formation--a hypothesis. Biol Chem. 2001;382(12):1629-36.
761 53. Mazat JP, Devin A, Ransac S. Modelling mitochondrial ROS production by the
762 respiratory chain. Cell Mol Life Sci. 2020;77(3):455-65.
763 54. Iwasaki A, Medzhitov R. Toll-like receptor control of the adaptive immune responses.
764 Nat Immunol. 2004;5(10):987-95.
765 55. Klinman DM. Immunotherapeutic uses of CpG oligodeoxynucleotides. Nat Rev Immunol.
766 2004;4(4):249-58.
767 56. Kwon HJ, Lee KW, Yu SH, Han JH, Kim DS. NF-kappaB-dependent regulation of tumor
768 necrosis factor-alpha gene expression by CpG-oligodeoxynucleotides. Biochem Biophys Res
769 Commun. 2003;311(1):129-38.
770 57. Lee KW, Kim DS, Kwon HJ. CG sequence- and phosphorothioate backbone
771 modification-dependent activation of the NF-kappaB-responsive gene expression by CpG-
772 oligodeoxynucleotides in human RPMI 8226 B cells. Mol Immunol. 2004;41(10):955-64.
773 58. Suwarti S, Yamazaki T, Svetlana C, Hanagata N. Recognition of CpG
774 oligodeoxynucleotides by human Toll-like receptor 9 and subsequent cytokine induction.
775 Biochem Biophys Res Commun. 2013;430(4):1234-9.
776 59. Brandt U. Bifurcated ubihydroquinone oxidation in the cytochrome bc1 complex by
777 proton-gated charge transfer. Febs Lett. 1996;387(1):1-6.

778 60. Hunte C, Palsdottir H, Trumpower BL. Protonmotive pathways and mechanisms in the
779 cytochrome bc1 complex. Febs Lett. 2003;545(1):39-46.
780 61. Quinlan CL, Gerencser AA, Treberg JR, Brand MD. The mechanism of superoxide
781 production by the antimycin-inhibited mitochondrial Q-cycle. J Biol Chem. 2011;286(36):31361-
782 72.
783 62. Sun J, Trumpower BL. Superoxide anion generation by the cytochrome bc1 complex.
784 Arch Biochem Biophys. 2003;419(2):198-206.
785 63. Rottenberg H, Covian R, Trumpower BL. Membrane potential greatly enhances
786 superoxide generation by the cytochrome bc1 complex reconstituted into phospholipid vesicles.
787 J Biol Chem. 2009;284(29):19203-10.
788 64. Federico A, Cardaioli E, Da Pozzo P, Formichi P, Gallus GN, Radi E. Mitochondria,
789 oxidative stress and neurodegeneration. J Neurol Sci. 2012;322(1-2):254-62.
790 65. Minelli A, Bellezza I, Conte C, Culig Z. Oxidative stress-related aging: A role for prostate
791 cancer? Biochim Biophys Acta. 2009;1795(2):83-91.
792 66. Asami DK, McDonald RB, Hagopian K, Horwitz BA, Warman D, Hsiao A, et al. Effect of
793 aging, caloric restriction, and uncoupling protein 3 (UCP3) on mitochondrial proton leak in mice.
794 Exp Gerontol. 2008;43(12):1069-76.
795 67. Lapointe J, Hekimi S. Early mitochondrial dysfunction in long-lived Mclk1+/- mice. J Biol
796 Chem. 2008;283(38):26217-27.
797 68. Lee SJ, Hwang AB, Kenyon C. Inhibition of respiration extends C. elegans life span via
798 reactive oxygen species that increase HIF-1 activity. Curr Biol. 2010;20(23):2131-6.
799 69. Scialo F, Sriram A, Fernandez-Ayala D, Gubina N, Lohmus M, Nelson G, et al.
800 Mitochondrial ROS Produced via Reverse Electron Transport Extend Animal Lifespan. Cell
801 Metab. 2016;23(4):725-34.
802 70. Yee C, Yang W, Hekimi S. The intrinsic apoptosis pathway mediates the pro-longevity
803 response to mitochondrial ROS in C. elegans. Cell. 2014;157(4):897-909.

804 71. Bai Y, Onuma H, Bai X, Medvedev AV, Misukonis M, Weinberg JB, et al. Persistent
805 nuclear factor-kappa B activation in Ucp2-/- mice leads to enhanced nitric oxide and
806 inflammatory cytokine production. J Biol Chem. 2005;280(19):19062-9.
807 72. Wang D, Malo D, Hekimi S. Elevated mitochondrial reactive oxygen species generation
808 affects the immune response via hypoxia-inducible factor-1alpha in long-lived Mclk1+/- mouse
809 mutants. J Immunol. 2010;184(2):582-90.
810 73. Wang D, Wang Y, Argyriou C, Carriere A, Malo D, Hekimi S. An enhanced immune
811 response of Mclk1(+)/(-) mutant mice is associated with partial protection from fibrosis, cancer
812 and the development of biomarkers of aging. PLoS One. 2012;7(11):e49606.
813 74. Han D, Antunes F, Canali R, Rettori D, Cadenas E. Voltage-dependent anion channels
814 control the release of the superoxide anion from mitochondria to cytosol. J Biol Chem.
815 2003;278(8):5557-63.
816 75. Muller FL, Liu Y, Van Remmen H. Complex III releases superoxide to both sides of the
817 inner mitochondrial membrane. J Biol Chem. 2004;279(47):49064-73.
818 76. You Y, Richer EJ, Huang T, Brody SL. Growth and differentiation of mouse tracheal
819 epithelial cells: selection of a proliferative population. Am J Physiol Lung Cell Mol Physiol.
820 2002;283(6):L1315-21.
821 77. Hemmi H, Takeuchi O, Kawai T, Kaisho T, Sato S, Sanjo H, et al. A Toll-like receptor
822 recognizes bacterial DNA. Nature. 2000;408(6813):740-5.
823 78. Okubo T, Knoepfler PS, Eisenman RN, Hogan BL. Nmyc plays an essential role during
824 lung development as a dosage-sensitive regulator of progenitor cell proliferation and
825 differentiation. Development. 2005;132(6):1363-74.
826 79. Fasbender A, Lee JH, Walters RW, Moninger TO, Zabner J, Welsh MJ. Incorporation of
827 adenovirus in calcium phosphate precipitates enhances gene transfer to airway epithelia in vitro
828 and in vivo. J Clin Invest. 1998;102(1):184-93.

80. Cordero-Reyes AM, Gupte AA, Youker KA, Loebe M, Hsueh WA, Torre-Amione G, et al. Freshly isolated mitochondria from failing human hearts exhibit preserved respiratory function. J Mol Cell Cardiol. 2014;68:98-105.

81. Brautbar A, Wang J, Abdenur JE, Chang RC, Thomas JA, Grebe TA, et al. The mitochondrial 13513G>A mutation is associated with Leigh disease phenotypes independent of complex I deficiency in muscle. Mol Genet Metab. 2008;94(4):485-90.

82. Enns GM, Hoppel CL, DeArmond SJ, Schelley S, Bass N, Weisiger K, et al. Relationship of primary mitochondrial respiratory chain dysfunction to fiber type abnormalities in skeletal muscle. Clin Genet. 2005;68(4):337-48.

83. Vu TH, Sciacco M, Tanji K, Nichter C, Bonilla E, Chatkupt S, et al. Clinical manifestations of mitochondrial DNA depletion. Neurology. 1998;50(6):1783-90.

84. Tibes R, Qiu Y, Lu Y, Hennessy B, Andreeff M, Mills GB, et al. Reverse phase protein array: validation of a novel proteomic technology and utility for analysis of primary leukemia specimens and hematopoietic stem cells. Mol Cancer Ther. 2006;5(10):2512-21.

85. Hu J, He X, Baggerly KA, Coombes KR, Hennessy BT, Mills GB. Non-parametric quantification of protein lysate arrays. Bioinformatics. 2007;23(15):1986-94.

Acknowledgements: Supported by U.S. National Institutes of Health grants R01 HL117976, DP2 HL123229, and R35 HL144805 to S.E.E. and grants S10 OD012304-01 and P30 CA016672 to the Metabolomics Core Facility.

Competing interests: MJT and SEE are authors on U.S. patent 8,883,174, “Stimulation of Innate Resistance of the Lungs to Infection with Synthetic Ligands.” MJT and SEE own stock in Pulmotect, Inc.

Data and materials availability: The datasets generated for the Reverse-phase protein array data is available in the Evans Laboratory GitHub repository (www.github.com/evanslaboratory/Datasource). Further data information is available upon reasonable requests and should be directed to and will be fulfilled by the corresponding author, Scott E. Evans (seevans@mdanderson.org).

Figure Legends

Fig. 1. Induction of epithelial mtROS by CpG ODN.

(**A**) mtROS production from HBEC3-KT cells after treatment with pathogen associated molecular patterns. (**B**) mtROS production from HBEC3-KT cells after treatment with the indicated ODNs. mtROS production after treatment with ODN from mouse lung epithelial cell lines (**C**) and primary human (**D**) and primary mouse (**E**) lung epithelial cells. (**F**) Representative fluorescence images primary tracheal epithelial cells harvested from mt-roGFP mice treated with PBS or ODN. Images shown as gradient of color intensity from the reduced (blue) form to the oxidized (green) form of roGFP. Scale bar, 50 μm. (**G**) Ratio of the fluorescence intensity of the oxidized:reduced roGFP from **F,** quantified at 488 nm and 405 nm, respectively. (**H**) Oxygen consumption following the indicated treatment by Seahorse XFe96 Flux Analyzer, shown as mean ± SEM. (**I**) Mitochondrial membrane potential $\Delta\psi_m$ measurement in HBEC3-KT cells after ODN treatment. * $p<0.001$ vs. PBS by one-way ANOVA using Holm-Sidak method, except A which use Tukey method due to failed normality testing; † $p<0.001$ vs PBS by two-way Student's t test. ODN, oligodeoxynucleotide; ISD, immune stimulating DNA; mTEC, primary mouse tracheal epithelial cells; NHBE, primary normal human bronchial epithelial cells; GFP, green fluorescent protein; OCR, oxygen consumption rate; TMRM, tetramethylrhodamine.

878 **Fig. 2**. **Mitochondrial energy metabolism altered by CpG ODN.**

879 (**A**) Summary electron transport chain complex enzyme activity with ODN treatment of HBEC3-
880 KT cells. (**B**) Mitochondrial protein immunoblots from lysates of cells treated with ODN. Relative
881 abundance ATP (**C**), ADP (**D**), and AMP (**E**) in whole cell lysates at the indicated time points
882 after ODN treatment. Relative abundance of NADH (**F**) an NADPH (**G**) in whole cells after ODN
883 treatment. (**H**) Ratio of reduced:oxidized glutathione in HBEC3-KT cells treated with ODN. *
884 $p<0.003$ vs PBS; † $p<0.001$ vs PBS. SDHB, succinate dehydrogenase subunit B; COX4,
885 cytochrome c oxidase subunit IV; ATP5A, ATP synthase subunit alpha; CS, citrate synthase;
886 VDAC1, voltage dependent anion channel 1; GSH, reduced glutathione; GSSG, oxidized
887 glutathione.

Fig. 3. Blocking mitochondrial nucleotide transition by CpG ODN leads to generation of antimicrobial mtROS.

(**A**) mtROS production and (**B**) $\Delta\psi_m$ increase in isolated mitochondria that were treated with Pam2, ODN or both. (**C**) Fluorescence intensity of mitochondria isolated from HBEC3-KT cells treated with FITC-labeled or unlabeled ODN. (**D**) Mitochondria were isolated from the biotinylated ODN-treated HBEC3-KT cells, and streptavidin precipitants from mitochondrial lysates were resolved by polyacrylamide gel electrophoresis and silver stained. Dashed line indicates bands excised for mass spectrometry analysis. As in **D**, streptavidin precipitants were probed for VDAC1 in mitochondrial lysates from (**E**) human or (**F**) mouse cells following treatment with ODN for the indicated time. Mitochondrial lysates from human cells were precipitated and probed for ANT1 (**G**) following treatment with ODN for the indicated time. (**H**) Representative images of HBEC3-KT cells treated with FITC-labeled ODN then stained with Alexa Fluor 555-labeled anti-VDAC1 antibody. Scale bar, 100 μm. (**I**) Measurements of cytosolic and mitochondrial levels of ATP, ADP & AMP in ODN-treated HBEC3-KT cells at the indicated times. Mitochondrial membrane potential $\Delta\psi_m$ (**J**) and mtROS (**K**) 100 min after HBEC3-KT treatment with the indicated mitochondrial permeability modulators. (**L**) Seahorse analysis of oxygen consumption following the indicated mitochondrial permeability modulators in oligomycin-inhibited HBEC3-KT cells, shown as mean ± SEM. * $p<0.001$ vs PBS by ANOVA; † $p<0.001$ vs unlabeled ODN by two-way Student's t test. Mito, mitochondria; VDAC1, voltage dependent anion channel 1; ANT1, adenine nucleotide translocator 1; CsA, cyclosporin A; CAT, carboxyatractyloside; OCR, oxygen consumption rate.

Fig. 4. **AMPK-regulated metabolic reprogram increases electron delivery to complex II.**

(**A**) RPPA heatmap from HBEC3-KT cells treated with PBS or ODN. (**B**) Immunoblot of AMPK and ACC proteins after ODN treatment. (**C**) Immunoblot for phospho-AMPKα1 following treatment with the indicated mitochondrial permeability modulators in HBEC3-KT cells. (**D**) Phospho-AMPK immunofluorescence in mouse lungs after treatment with ODN. Scale bar, 50 μm. (**E**) Quantification of fluorescence in **D**. (**F**) mtROS production in primary *Prkaa1*$^{fl/fl}$*;Prkka2*$^{fl/fl}$ mouse tracheal epithelial cells infected with empty or Cre^{+} adenovirus, then treated with PBS or ODN. (**G**) Acetyl-CoA levels in ODN-treated HBEC3-KT cells. (**H**) Fatty acid oxidation after ODN treatment. (**I**) mtROS production following treatment with ODN and/or β-oxidation inhibitor etomoxir. (**J**) Oxygen consumption following the indicated treatments, shown as mean ± SEM. (**K**) HBEC3-KT cell complex II activity following treatment with the indicated agents.ODN-induced mtROS production in cells with knockdowns of gene CPT1A (**L**) and the genes for electron shuttles GPD2 (**M**) or ETFDH (**N**). (**O**) Ratio of reduced:oxidized CoQ in mitochondria isolated from HBEC3-KT cells treated with PBS or ODN. (**P**) Schematic model of mtROS formation induced by ODN via metabolic reprogramming. * $p < 0.01$ vs 0 min; † $p < 0.001$ vs. (syngeneic) PBS treated; ‡ $p < 0.02$ vs (syngeneic) PBS treated. RPPA, reverse phase protein array; AMPK, AMP-activating protein kinase; ACC, acetyl-CoA carboxylase; AdV, adenovirus; OCR, oxygen consumption rate; Scr, scrambled shRNA control; CPT1A, carnitine palmitoyltransferase 1A; GPD2, glycerol-3-phosphate dehydrogenase 2; ETFDH, electron transfer flavoprotein-ubiquinone dehydrogenase.

Fig. 5. mtROS formation at complex III is ΔΨm-dependent.

(**A**) Electron transport chain complex III activity in HBEC3-KT cells 100 min after ODN or antimycin treatment. (**B**) mtROS production 100 min after the indicated treatments. (**C**) Oxygen consumption following the indicated treatments in stigmatellin and myxothiazol-inhibited HBEC3-KT cells, shown as mean ± SEM. Time course of mtROS generation following PBS, ODN or antimycin treatment in (**D**) HBEC3-KT cells or (**E**) isolated mitochondria. Time-dependent mitochondrial membrane potential in (**F**) HBEC3-KT cells or (**G**) isolated mitochondria. Mitochondrial membrane potential $\Delta_{\psi m}$ 100 min after ODN or antimycin treatments in (**H**) HBEC3-KT cells or (**I**) isolated mitochondria with or without FCCP pre-treatment. mtROS generation 100 min after ODN or antimycin treatments in (**J**) HBEC3-KT cells or (**K**) isolated mitochondria with or without FCCP pre-treatment. (**L**) Reduced mitochondrial complex III cytochrome b_H levels following ODN or antimycin treatment with or without FCCP pre-treatment, expressed relative to DTT-treated mitochondria (DTT-treated presumed 100% reduced). (**M**) Complex III activity in isolated mitochondria 15 min after the indicated treatments. (**N**) Schematic model of $\Delta_{\psi m}$-dependent mtROS formation at complex III. * $p<0.001$ vs PBS by ANOVA; † $p<0.008$ vs ODN + antimycin treated by ANOVA; ‡ $p<0.02$ vs PBS by ANOVA. mito, mitochondria; DTT, dithiothreitol.

947 **Fig. 6. mtROS induction stimulates antimicrobial responses.**

948 (**A**) Representative fluorescence images primary tracheal epithelial cells harvested from mt-
949 roGFP mice, pre-treated (or not) with TTFA and FCCP, then treated with PBS or ODN. Images
950 shown as gradient of color intensity from the reduced (blue) form to the oxidized (green) form of
951 roGFP. Scale bar, 50 μm. (**B**) Ratio of the fluorescence intensity of the oxidized:reduced roGFP
952 from **A,** quantified at 488 nm and 405 nm, respectively. (**C**) Bacterial burden of HBEC3-KT cells
953 treated with the indicated ligands with or without TTFA-FCCP treatment. (**D**) Survival of wild
954 type mice challenged with *P. aeruginosa* one day after nebulized treatment with PBS or Pam2
955 and ODN with or without TTFA-FCCP (n=15 mice/group). (**E**) Survival of *Tlr9*$^{-/-}$ mice challenged
956 with *P. aeruginosa* one day after nebulized treatment with PBS or Pam2 and ODN with or
957 without TTFA-FCCP (n=15 mice/group). (**F**) Bacterial burden of HBEC3-KT cells treated with
958 Pam2 and erastin or ODN. (**G**) Mouse survival of *P. aeruginosa* challenge given one day after
959 nebulized treatment with the indicated agents (n=15 mice/group). (**H**) Mouse lung bacterial
960 burden immediately after *P. aeruginosa* challenge following treatment with the indicated agents
961 (n=4 mice/group). * p <0.02 vs PBS, † p< 0.05 vs ODN, ‡ p < 0.05 vs same ligand without
962 TTFA-FCCP, ¶ P <0.0001 vs. PBS.

963

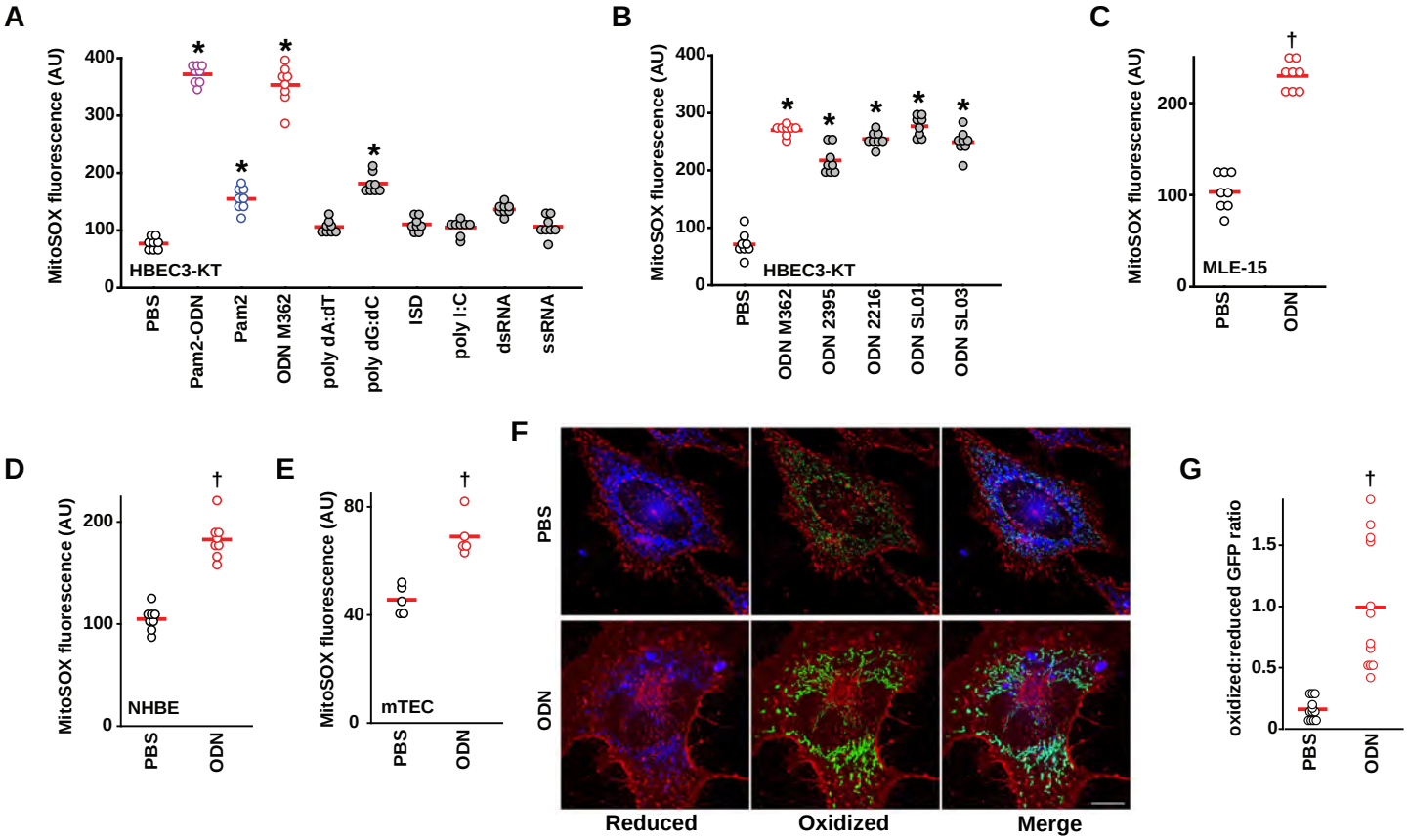

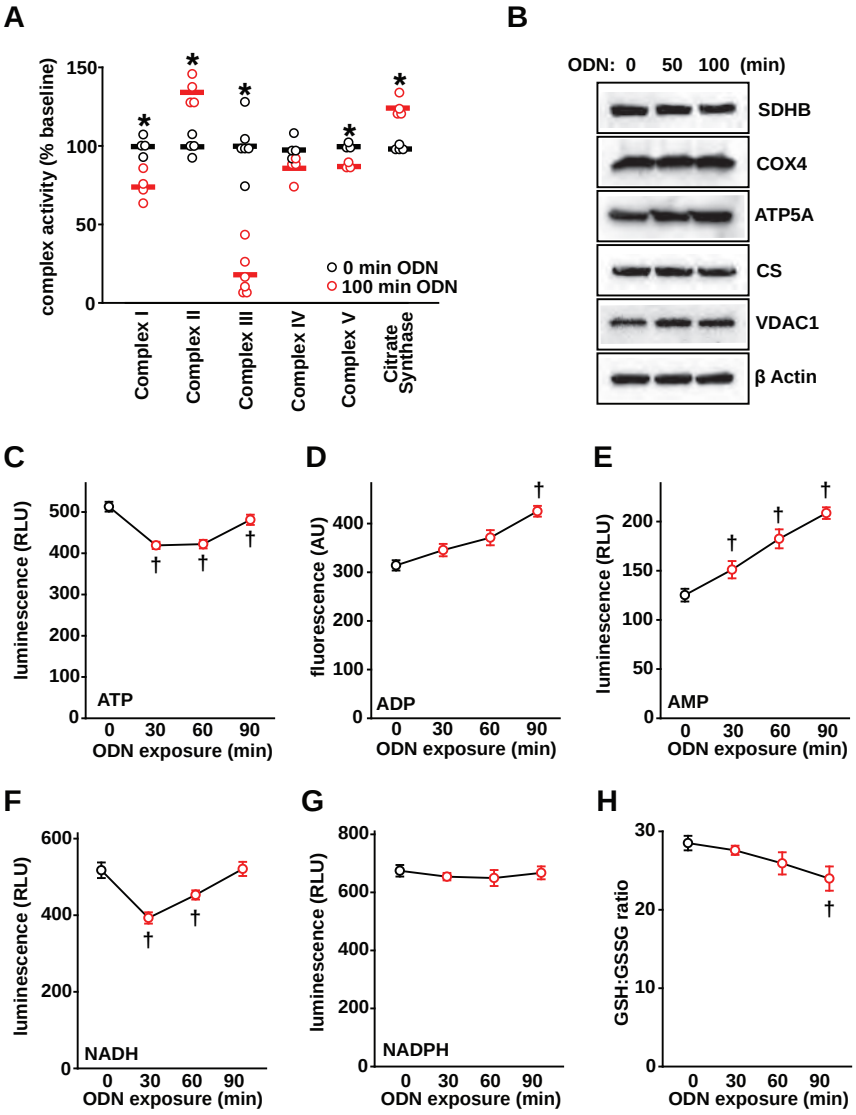

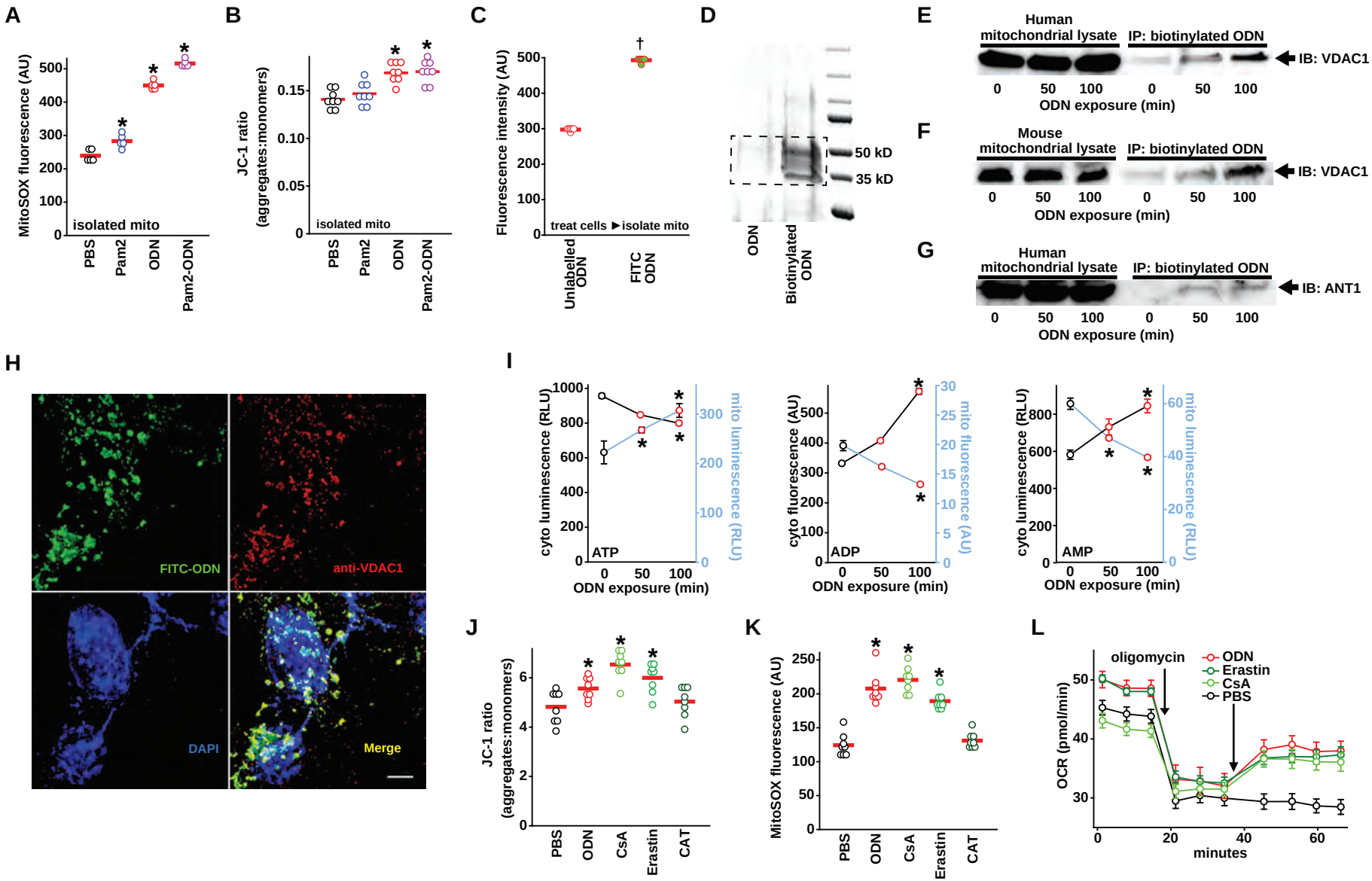
A
MitoSOX fluorescence (AU)
isolated mito
PBS
Pam2
ODN
Pam2-ODN
B
JC-1 ratio (aggregates:monomers)
isolated mito
C
Fluorescence intensity (AU)
treat cells ►isolate mito
Unlabelled ODN
FITC ODN
D
50 kD
35 kD
ODN
Biotinylated ODN
E
Human mitochondrial lysate
IP: biotinylated ODN
IB: VDAC1
ODN exposure (min)
F
Mouse mitochondrial lysate
IP: biotinylated ODN
IB: VDAC1
ODN exposure (min)
G
Human mitochondrial lysate
IP: biotinylated ODN
IB: ANT1
ODN exposure (min)
H
FITC-ODN
anti-VDAC1
DAPI
Merge
I
cyto luminescence (RLU)
mito luminescence (RLU)
ATP
ODN exposure (min)
cyto fluorescence (AU)
mito fluorescence (AU)
ADP
ODN exposure (min)
cyto luminescence (RLU)
mito luminescence (RLU)
AMP
ODN exposure (min)
J
JC-1 ratio (aggregates:monomers)
PBS
ODN
CsA
Erastin
CAT
K
MitoSOX fluorescence (AU)
PBS
ODN
CsA
Erastin
CAT
L
oligomycin
ODN
Erastin
CsA
PBS
OCR (pmol/min)
minutes

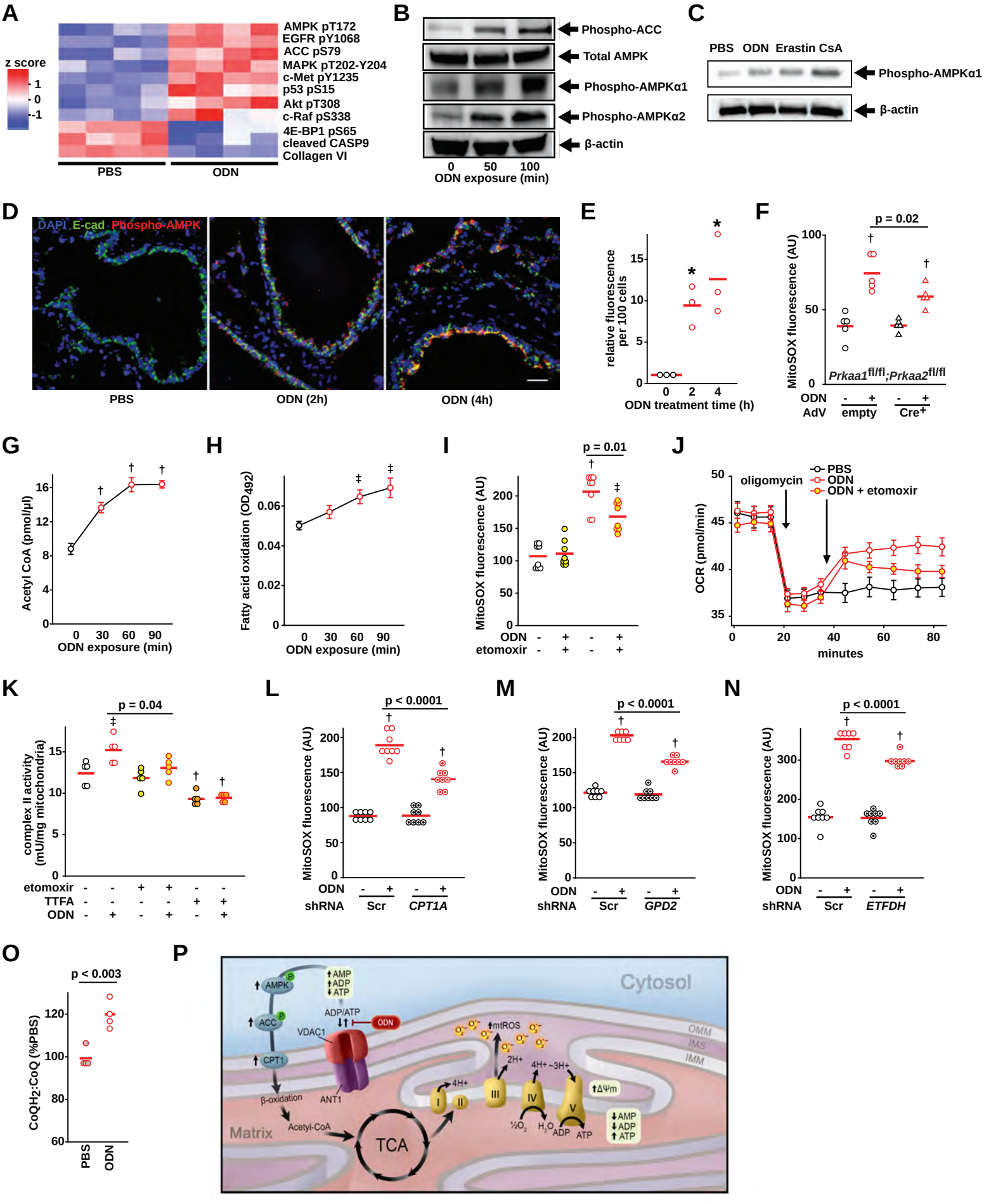

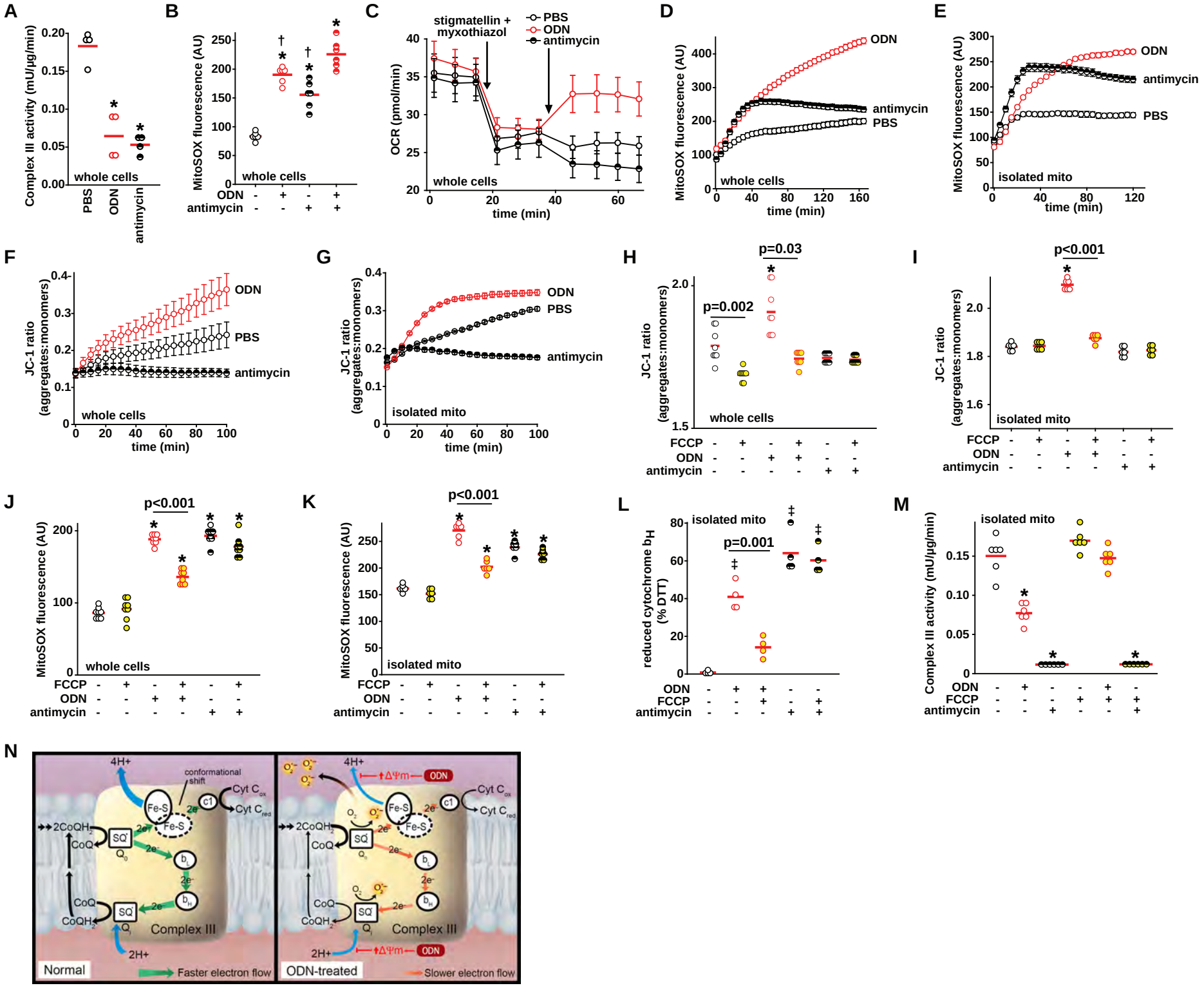
A
Complex III activity (mU/µg/min)
whole cells
PBS
ODN
antimycin
B
MitoSOX fluorescence (AU)
whole cells
ODN
antimycin
C
stigmatellin + myxothiazol
PBS
ODN
antimycin
OCR (pmol/min)
whole cells
time (min)
D
MitoSOX fluorescence (AU)
ODN
antimycin
PBS
whole cells
time (min)
E
MitoSOX fluorescence (AU)
ODN
antimycin
PBS
isolated mito
time (min)
F
JC-1 ratio (aggregates:monomers)
ODN
PBS
antimycin
whole cells
time (min)
G
JC-1 ratio (aggregates:monomers)
ODN
PBS
antimycin
isolated mito
time (min)
H
p=0.03
p=0.002
JC-1 ratio (aggregates:monomers)
whole cells
FCCP
ODN
antimycin
I
p<0.001
JC-1 ratio (aggregates:monomers)
isolated mito
FCCP
ODN
antimycin
J
p<0.001
MitoSOX fluorescence (AU)
whole cells
FCCP
ODN
antimycin
K
p<0.001
MitoSOX fluorescence (AU)
isolated mito
FCCP
ODN
antimycin
L
isolated mito
p=0.001
reduced cytochrome bH (% DTT)
ODN
FCCP
antimycin
M
isolated mito
Complex III activity (mU/µg/min)
ODN
FCCP
antimycin
N
4H+
conformational shift
Fe-S
c1
Cyt Cox
Cyt Cred
2CoQH2
CoQ
SQ
Q0
bL
bH
Qi
Complex III
2H+
Normal
Faster electron flow
ODN
ΔΨm
ODN-treated
Slower electron flow

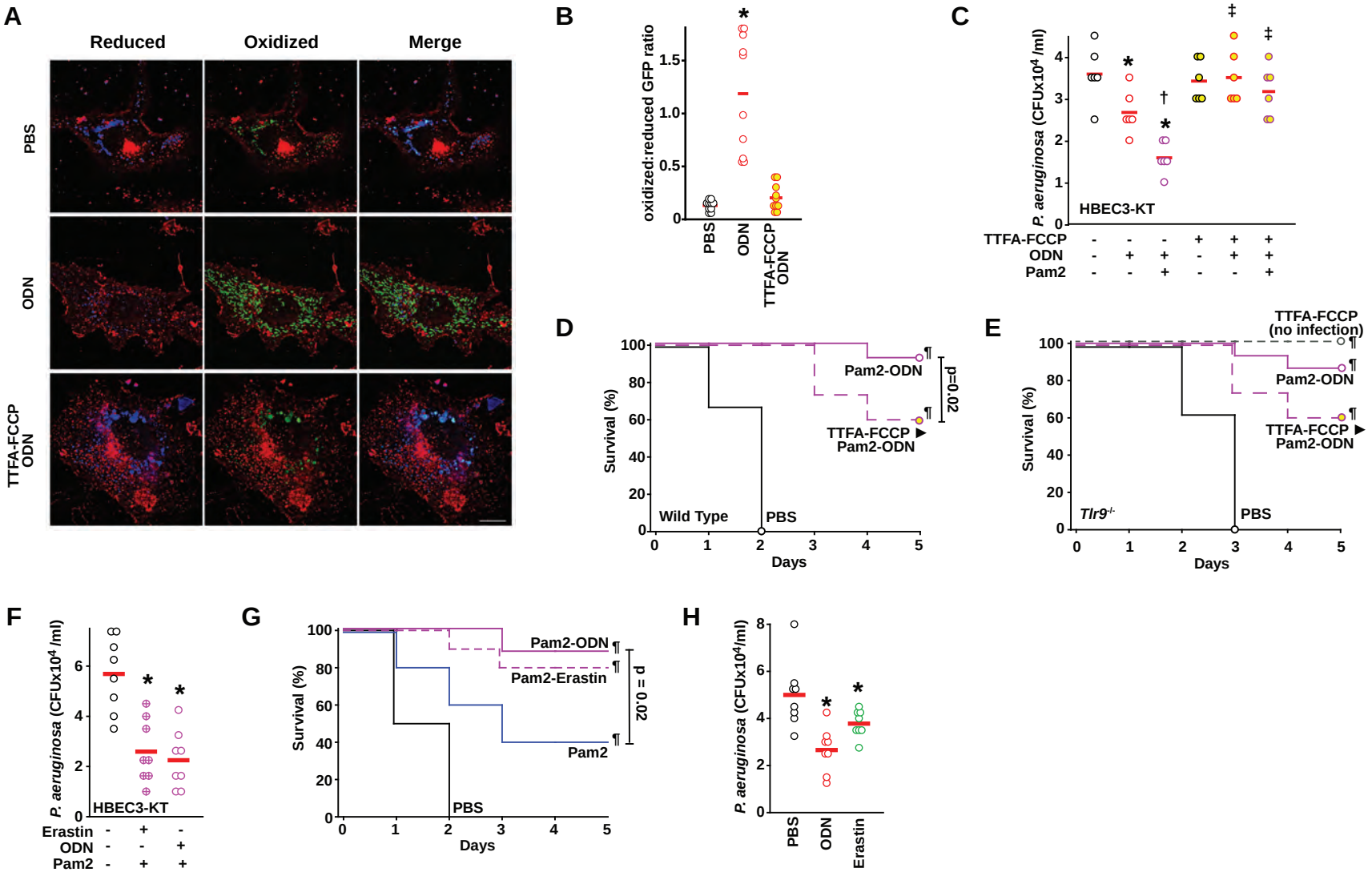
A
Reduced
Oxidized
Merge
PBS
ODN
TTFA-FCCP ODN
B
oxidized:reduced GFP ratio
PBS
ODN
TTFA-FCCP ODN
C
P. aeruginosa (CFUx10⁴ /ml)
HBEC3-KT
TTFA-FCCP
ODN
Pam2
D
Survival (%)
Pam2-ODN
TTFA-FCCP ▶ Pam2-ODN
p=0.02
Wild Type
PBS
Days
E
TTFA-FCCP (no infection)
Pam2-ODN
TTFA-FCCP ▶ Pam2-ODN
Tlr9-/-
PBS
Survival (%)
Days
F
P. aeruginosa (CFUx10⁴ /ml)
HBEC3-KT
Erastin
ODN
Pam2
G
Survival (%)
Pam2-ODN
Pam2-Erastin
Pam2
p = 0.02
PBS
Days
H
P. aeruginosa (CFUx10⁴/ml)
PBS
ODN
Erastin